Mutual Information-Based Trajectory Planning for Cislunar Space Object Tracking using Successive Convexification

Trevor N. Wolf*, David Fridovich-Keil†, and Brandon A. Jones‡
The University of Texas at Austin, Austin, Texas, 78712

We consider the problem of trajectory planning for optimal relative orbit determination in the cislunar environment. The recent interest in cislunar space has created a need to develop autonomous tracking technologies that can maintain situational awareness of this dynamically complex regime. Optical sensors provide an ideal observation platform because of their low cost and versatility in tracking both cooperative and non-cooperative space objects. The estimation performance of an optical observer can be significantly enhanced through manuevering. This work develops a trajectory planning tool, compatible with low-thrust propulsion, for tracking one or multiple targets operating in proximity to the observer. We formulate an objective function that is a convex combination of the mutual information between target states and measurements, and the low-thrust control effort. The subsequent optimal control problem is solved via direct collocation using the successive convexification algorithm which, we argue, is well suited for a potential onboard trajectory planning application. We demonstrate the tool for several relevant scenarios with one and multiple targets operating in periodic orbits in the circular restricted three-body problem. A sequential estimator's performance is evaluated using the Cramer-Rao lower bound and, compared to a purely passive observer, we show that optimizing the observer's trajectory can decrease this bound by up to several orders of magnitude within a planning window. This investigation provides an initial proof-of-concept to future onboard planning technologies for relative tracking in the cislunar domain.

I. Introduction

THE region between the Earth and the moon opens possibilities for many unique mission architectures, however, the non-linear dynamics in cislunar space coupled with its vast volume make situational awareness infeasible with solely Earth-based sensing resources. There is no shortage of both public and private organizations eager to establish a presence in this domain and, inevitably, this growth will congest the environment in a manner similar to Earth orbit. Moreover, tracking in cislunar space is only tangible with exquisite Earth-based facilities such as the Deep Space Network (DSN), and the expected growth will far out-pace its current capacity. For these reasons, there is a critical need to develop technologies for autonomous tracking and navigation that can operate in cislunar space. Sensing platforms will need to perform mission planning with little operator intervention to achieve mission objectives. For instance, it is desirable for a spacecraft to receive an abstract goal (e.g., maintain a desired definition of custody for an object catalog) and then autonomously determine and execute a mission profile that can achieve such an objective [1].

Electro-optical sensors are an ideal measurement mode for their utility in tracking both cooperative and non-cooperative space objects. They rely solely on reflected light from the sun so are not power limited, and can operate at greater ranges. Optical sensors map pixel coordinates from the sensor plane into angular bearings either in a local or inertial frame of reference. The measurements provide partial state information, but taken individually, do not fully observe the state of the system. Series of angular bearings observed from a sensing platform and processed by sequential filters are effective for orbit determination and navigation in astronautical applications (e.g., [2], [3]). More recent work has investigated their feasibility in the cislunar domain. In [4] the authors investigate optical-only navigation with features including lunar landmarks, lunar asteroids, and artificial satellites. [5] conducts a comparison between different combinations of observation modalities for navigation in a near-rectilinear halo orbit (NRHO). In [6] the authors characterize the performance of an optical observer located at different periodic orbits for cislunar Space Situational Awareness (SSA).

---

*Graduate Research Assistant, Department of Aerospace Engineering & Engineering Mechanics, AIAA Student Member
†Assistant Professor, Department of Aerospace Engineering & Engineering Mechanics
‡Associate Professor, Department of Aerospace Engineering & Engineering Mechanics, AIAA Associate Fellow

Reconfiguring a mobile optical sensor can significantly enhance the observability of the system. Early work such as [7] evaluated the effect of course maneuvers on state estimation performance using the Cramer-Rao lower bound (CRLB). Both [8] and [9] develop analytic expressions for optimal maneuvers based on geometric definitions of observability for optical navigation applications in Earth orbit. These definitions, however, do not fully encapsulate the effect of a maneuver on a state estimator over extended time intervals. Alternatively, there has been considerable work in optimizing motion planning with respect to measures that directly relate to an estimator's performance. Among these, the Fisher information matrix (FIM) is extensively utilized in the literature (e.g., [10], [11], [12]). The FIM is the inverse of the CRLB which, for a linear/Gaussian system, provides the asymptotic error covariance for an unbiased estimator. For a nonlinear system, the FIM however is only a local estimate of the information. On the other hand, the mutual information, defined as the Kullback-Leibler (KL) divergence between a prior and posterior state distributions, provides a consistent information measure for nonlinear/non-Gaussian systems that is a function of the entire probability density function (PDF) [13].

This work develops a mutual information-based trajectory planning algorithm for the purpose of relative target tracking around periodic orbits in the circular restricted three-body problem (CRTBP) compatible with a low-thrust mobile observer. We formulate an objective that is convex combination of the control effort and the mutual information for one or multiple space objects acquired over a finite time horizon. The associated optimal control problem is solved with direct collocation using sequential convex programming (SCP). More specifically, we use the successive convexification (SCvx) algorithm [14, 15]. State-of-the-art SCP algorithms are appealing because they are robust to a coarse initial solution guess, require very few solver iterations, and are amenable to off-the-shelf convex programming solvers. Moreover, unlike sequential quadratic program (SQP) solvers, they do not require the computation of second order derivatives which can be computationally expensive. For these reasons, SCP algorithms can be employed in real-time for tasks such as powered descent guidance [16, 17] and model predictive control for spacecraft swarms [18]. Related to this work, [19] employs an SCP algorithm for mission planning in transferring between a halo orbit and NRHO. The authors show that their SCP algorithm can successfully converge to an optimal solution, despite the highly nonlinear and unstable dynamics.

The rest of this work is organized as follows: In Section II we describe the derivation of the mutual information objective used for optimizing the motion of the sensing platform. We also summarize the equations of motion and the measurement model of the observer. Section III details our implementation of the SCvx algorithm. In this, we formulate an optimal control problem where the objective is to minimize a convex combination of the mutual information and control effort, and we provide a necessary description for implementation. Additionally, we describe a regularization for spacing collocation nodes that better facilitates solution convergence. We demonstrate several numerical simulations in Section IV for NRHO and DRO periodic orbits for single and multiple target tracking and compare a spectrum of solutions by varying the homotopy parameter controlling the relative importance of control effort and mutual information. The estimation performance is evaluated by comparing the CRLB with a passive observer. Finally, in Section V we summarize our main contributions in this work and suggest ideas future investigations.

II. Problem Formulation

A. Formulating the Objective Function

In this section, our goal is to formulate an objective function that properly encapsulates a sequential estimator's performance in tracking N_{T} objects from a mobile platform over an entire planning window. The transitional dynamics for each of the targets, indexed by the superscript i, between discrete measurement time steps k and $k + 1$ is given by

$$x_{\mathrm{T},k+1}^{(i)} = f_k^{(i)}(x_{\mathrm{T},k}^{(i)}) + v_k^{(i)}, \quad \text{for } i = 1, 2, \cdots, N_{\mathrm{T}}. \tag{1}$$

Note that in this work we use the subscript "T" to explicitly denote variables that are associated to a target. This is to mitigate any confusion with variables belonging to the sensing platform. Additionally, the discretization used in Section III does not correspond to the measurement time steps, $k = 1, 2, \cdots, N_{\mathrm{meas}}$, used in this section, where N_{meas} is the number of measurements collected. $x_{\mathrm{T},k}^{(i)} \in \mathbb{R}^{n_x}$ is the state of the ith target at time step k, $f_k^{(i)}(\cdot)$ is a discrete time representation of the system dynamics between step k and $k + 1$, and $v_k^{(i)}$ is the process noise, where $v_k^{(i)} \sim \mathcal{N}(v_k^{(i)}; \mathbf{0}, Q_k^{(i)})$. Here, $\mathcal{N}(\cdot; \mathbf{m}, P)$ denotes a Gaussian distribution with mean $\mathbf{m}$ and covariance P.

We assume measurements of all targets are obtained synchronously from the mobile sensing platform and are given

2

by

$$y_k^{(i)} = h(x_{T,k}^{(i)}, x_k) + w_k, \quad \text{for } i = 1, 2, \cdots, N_T, \tag{2}$$

where $y_k^{(i)} \in \mathbb{R}^{n_y}$ is the measurement of target i at time step k. In the above, we explicitly include the dependence of the mobile sensor's state, x_k, in the measurement function, $h(\cdot, \cdot)$, to highlight that this dependence is exploited to maximize the performance of the observer. w_k is the measurement noise, where $w_k \sim \mathcal{N}(w_k; \mathbf{0}, R)$.

The objective of the observer is to plan a trajectory such that the mutual information between the targets' measurements and states is maximized. Each of the targets are assumed independent and so the mutual information for each can be calculated independently. For a given step k, the mutual information for target i is

$$I^{(i)}(x_{T,k}^{(i)}; y_k^{(i)}) = \mathcal{D}_{KL}\left(p(x_{T,k}^{(i)}, y_k^{(i)}) \| p(x_{T,k}^{(i)}) p(y_k^{(i)})\right), \tag{3}$$

where $\mathcal{D}_{KL}(\cdot \| \cdot)$ is the KL divergence defined as

$$\mathcal{D}_{KL}(p(x) \| q(x)) = \int_{-\infty}^{\infty} p(x) \ln\left(\frac{p(x)}{q(x)}\right) dx, \tag{4}$$

for arbitrary continuous distributions $p(x)$ and $q(x)$, where the distribution $q(x)$ has full support. The KL divergence is commonly interpreted as measure of dissimilarity between probability distributions. Inspecting Eq. 3, maximizing the mutual information amounts to maximizing the dissimilarity between the joint and product of conditionally independent distributions for the state and measurement. Additionally, by marginalizing the joint distribution, Eq. 3 is equivalent to

$$\begin{aligned} I^{(i)}(x_{T,k}^{(i)}; y_k^{(i)}) &= \mathbb{E}_{y_k^{(i)}} \left[\mathcal{D}_{KL}\left(p(x_{T,k}^{(i)} | y_k^{(i)}) \| p(x_{T,k}^{(i)})\right) \right] \\ &= \mathbb{E}_{x_{T,k}^{(i)}} \left[\mathcal{D}_{KL}\left(p(y_k^{(i)} | x_{T,k}^{(i)}) \| p(y_k^{(i)})\right) \right]. \end{aligned} \tag{5}$$

Therefore, maximizing the mutual information is the same as maximizing the expected dissimilarity between a prior and posterior distribution when the expectation is taken with respect to the data variable. This has a rather nice intuitive explanation as any conditional distribution will contain the same or greater information content for a parameter than the conditionally independent distribution of the parameter. For this reason, the mutual information between the state and measurement variables is sometimes referred to as the information gain [20].

Rather than maximizing the mutual information at one time step, we would like to maximize it along the entire trajectory. We assume that the states and measurements for target i along the trajectory is jointly Gaussian so that

$$p\left(X_T^{(i)}, Y^{(i)}\right) = \mathcal{N}\left(\begin{bmatrix} X_T^{(i)} \\ Y^{(i)} \end{bmatrix}; \begin{bmatrix} \hat{X}_T^{(i)} \\ \hat{Y}^{(i)} \end{bmatrix}, \tilde{\Sigma}^{(i)}\right) \tag{6}$$

where,

$$X_T^{(i)} = [x_{T,1}^{(i)\top}, x_{T,2}^{(i)\top}, \cdots, x_{T,N_{meas}}^{(i)\top}]^\top, \tag{7}$$

$$Y^{(i)} = [y_1^{(i)\top}, y_2^{(i)\top}, \cdots, y_{N_{meas}}^{(i)\top}]^\top, \tag{8}$$

and,

$$\tilde{\Sigma}^{(i)} = \mathbb{E}\left[\left(\begin{bmatrix} X_T^{(i)} \\ Y^{(i)} \end{bmatrix} - \begin{bmatrix} \hat{X}_T^{(i)} \\ \hat{Y}^{(i)} \end{bmatrix}\right)\left(\begin{bmatrix} X_T^{(i)} \\ Y^{(i)} \end{bmatrix} - \begin{bmatrix} \hat{X}_T^{(i)} \\ \hat{Y}^{(i)} \end{bmatrix}\right)^\top\right]. \tag{9}$$

Here, $\hat{X}_T^{(i)}$ and $\hat{Y}^{(i)}$ are the augmented predicted state and measurements along the trajectory arc, respectively. There are several ways to compute the expectation integral in Eq. 9. In [13] the authors use sigma points with the conjugate unscented transform. In this work, we choose to approximate the expectation using a first order Taylor series expansion so that

$$\tilde{\Sigma}^{(i)} = \begin{bmatrix} \tilde{P}^{(i)} & \tilde{\Gamma}^{(i)} \\ \tilde{\Gamma}^{(i)\top} & \tilde{S}^{(i)} \end{bmatrix} = \begin{bmatrix} \tilde{\Phi}_T^{(i)} \tilde{Q}^{(i)} \tilde{\Phi}_T^{(i)\top} & \tilde{\Phi}_T^{(i)} \tilde{Q}^{(i)} \tilde{H}^{(i)\top} \\ \tilde{H}^{(i)} \tilde{Q}^{(i)} \tilde{\Phi}_T^{(i)\top} & \tilde{H}^{(i)} \tilde{Q}^{(i)} \tilde{H}^{(i)\top} + \tilde{R} \end{bmatrix}. \tag{10}$$

3

The block matrices that form Eq. 10 are given as

$$\tilde{Q}^{(i)} = \begin{bmatrix} P_1^{(i)} & 0_{n_x \times n_x} & \cdots & 0_{n_x \times n_x} \\ 0_{n_x \times n_x} & Q_1^{(i)} & \cdots & 0_{n_x \times n_x} \\ \vdots & \vdots & \ddots & \vdots \\ 0_{n_x \times n_x} & 0_{n_x \times n_x} & \cdots & Q_{N_{\text{meas}}-1}^{(i)} \end{bmatrix}, \tag{11}$$

$$\tilde{R} = \begin{bmatrix} R & 0_{n_y \times n_y} & \cdots & 0_{n_y \times n_y} \\ 0_{n_y \times n_y} & R & \cdots & 0_{n_y \times n_y} \\ \vdots & \vdots & \ddots & \vdots \\ 0_{n_y \times n_y} & 0_{n_y \times n_y} & \cdots & R \end{bmatrix}, \tag{12}$$

$$\tilde{\Phi}_{\text{T}}^{(i)} = \begin{bmatrix} I_{n_x \times n_x} & 0_{n_x \times n_x} & 0_{n_x \times n_x} & \cdots & 0_{n_x \times n_x} \\ \Phi_{\text{T}}^{(i)}(t_2, t_1) & I_{n_x \times n_x} & 0_{n_x \times n_x} & \cdots & 0_{n_x \times n_x} \\ \Phi_{\text{T}}^{(i)}(t_3, t_1) & \Phi_{\text{T}}^{(i)}(t_3, t_2) & I_{n_x \times n_x} & \cdots & 0_{n_x \times n_x} \\ \vdots & \vdots & \vdots & \ddots & \vdots \\ \Phi_{\text{T}}^{(i)}(t_{N_{\text{meas}}}, t_1) & \Phi_{\text{T}}^{(i)}(t_{N_{\text{meas}}}, t_2) & \Phi_{\text{T}}^{(i)}(t_{N_{\text{meas}}}, t_3) & \cdots & I_{n_x \times n_x} \end{bmatrix}, \tag{13}$$

and,

$$\tilde{H}^{(i)} = \begin{bmatrix} H_1^{(i)} & 0_{n_y \times n_x} & 0_{n_y \times n_x} & \cdots & 0_{n_y \times n_x} \\ H_2^{(i)}\Phi_{\text{T}}^{(i)}(t_2, t_1) & H_2^{(i)} & 0_{n_y \times n_x} & \cdots & 0_{n_y \times n_x} \\ H_3^{(i)}\Phi_{\text{T}}^{(i)}(t_3, t_1) & H_3^{(i)}\Phi_{\text{T}}^{(i)}(t_3, t_2) & H_3^{(i)} & \cdots & 0_{n_y \times n_x} \\ \vdots & \vdots & \vdots & \ddots & \vdots \\ H_{N_{\text{meas}}}^{(i)}\Phi_{\text{T}}^{(i)}(t_{N_{\text{meas}}}, t_1) & H_{N_{\text{meas}}}^{(i)}\Phi_{\text{T}}^{(i)}(t_{N_{\text{meas}}}, t_2) & H_{N_{\text{meas}}}^{(i)}\Phi_{\text{T}}^{(i)}(t_{N_{\text{meas}}}, t_3) & \cdots & H_{N_{\text{meas}}}^{(i)} \end{bmatrix}. \tag{14}$$

The matrices $\Phi_{\text{T}}^{(i)}(\cdot, \cdot) \in \mathbb{R}^{n_x \times n_x}$ and $H_k^{(i)} \in \mathbb{R}^{n_y \times n_x}$ are the state transition matrix and measurement partials, defined as

$$\Phi_{\text{T}}^{(i)}(t_{k+1}, t_k) = \frac{\partial \boldsymbol{f}_k^{(i)}(\boldsymbol{x}_{\text{T},k})}{\partial \boldsymbol{x}_{\text{T},k}^{(i)}}\bigg|_{\boldsymbol{x}_{\text{T},k}=\hat{\boldsymbol{x}}_{\text{T},k}}, \tag{15}$$

and,

$$H_k^{(i)} = \frac{\partial \boldsymbol{h}(\boldsymbol{x}_{\text{T},k}^{(i)}, \boldsymbol{x}_k)}{\partial \boldsymbol{x}_{\text{T},k}}\bigg|_{\boldsymbol{x}_{\text{T},k}=\hat{\boldsymbol{x}}_{\text{T},k}}, \tag{16}$$

respectively. $\hat{\boldsymbol{x}}_{\text{T},k}$ is the predicted target state at time step k. In Eq. 11, $P_1^{(i)}$ is the initial state error covariance associated to the target. The process noise covariance matrices are defined as

$$Q_k^{(i)} = Q^{(i)}(t_{k+1}, t_k) = \int_{t_k}^{t_{k+1}} \Phi^{(i)}(t, \tau)GQG^\top\Phi^{(i)}(t, \tau)^\top d\tau, \tag{17}$$

where Q is the process noise power spectral density (PSD), and $G = [0_{3\times3}, I_{3\times3}]^\top$ is the process noise gain matrix. In practice, we jointly compute the predicted target state, state transition matrix, and process noise covariance matrix by numerically integrating

$$\boldsymbol{\Psi}^{(i)}(t) = \begin{bmatrix} \hat{\boldsymbol{x}}_{\text{T}}^{(i)}(t) \\ \text{flat}\left(\Phi_{\text{T}}^{(i)}(t, t_k)\right) \\ \text{flat}\left(Q^{(i)}(t, t_k)\right) \end{bmatrix}, \tag{18}$$

where,

$$\dot{\boldsymbol{\Psi}}^{(i)}(t) = \begin{bmatrix} \boldsymbol{f}\left(\hat{\boldsymbol{x}}_{\text{T}}^{(i)}, t\right) \\ \text{flat}\left(A(t)\Phi_{\text{T}}^{(i)}(t, t_k)\right) \\ \text{flat}\left(\dot{Q}^{(i)}(t, t_k)\right) \end{bmatrix}, \quad \boldsymbol{\Psi}^{(i)}(t_k) = \begin{bmatrix} \hat{\boldsymbol{x}}_{\text{T},k}^{(i)} \\ \text{flat}(I_{n_x \times n_x}) \\ 0_{n_x n_x \times 1} \end{bmatrix}. \tag{19}$$

4

In the above, the operator $\text{flat}(\cdot)$ stacks the columns of a matrix into a vector. $\boldsymbol{f}(\cdot)$ is the continuous time dynamics equations. We note that previously we used discrete-time to naturally express the transitional dynamics in a filtering problem, however, the discrete time transition function $\boldsymbol{f}_k^{(i)}(\cdot)$ involves numerically integrating $\boldsymbol{f}(\cdot)$. $A(t)$ is the continuous time dynamics Jacobian matrix, and

$$\dot{Q}(t, t_k) = A(t)Q(t, t_k) + Q(t, t_k)A^\top(t) + \Gamma(t)Q\Gamma^\top(t). \tag{20}$$

Now, we are ready to provide the form of the mutual information used in this work. Because we assume $\boldsymbol{X}_{\mathrm{T}}^{(i)}$ and $\boldsymbol{Y}^{(i)}$ are jointly Gaussian, the mutual information in Eq. 3 possesses the close form expression,

$$\boldsymbol{I}^{(i)}(\boldsymbol{X}_{\mathrm{T}}^{(i)}; \boldsymbol{Y}_{\mathrm{T}}^{(i)}) = \frac{1}{2} \ln \left(\frac{|\tilde{P}^{(i)}||\tilde{S}^{(i)}|}{|\tilde{\Sigma}^{(i)}|} \right). \tag{21}$$

Similarly, using the Kalman filter covariance update, the conditional form of the mutual information in Eq. 5 can be expressed as

$$\begin{aligned}
\boldsymbol{I}^{(i)}(\boldsymbol{X}_{\mathrm{T}}^{(i)}; \boldsymbol{Y}^{(i)}) &= \frac{1}{2} \ln \left(\frac{|\tilde{S}^{(i)}|}{|\tilde{S}^{(i)} - \tilde{\Gamma}^{(i)\top} \left(\tilde{P}^{(i)} \right)^{-1} \tilde{\Gamma}^{(i)}|} \right) \\
&= \frac{1}{2} \ln \left(\frac{|\tilde{P}^{(i)}|}{|\tilde{P}^{(i)} - \tilde{\Gamma}^{(i)} \left(\tilde{S}^{(i)} \right)^{-1} \tilde{\Gamma}^{(i)\top}|} \right).
\end{aligned} \tag{22}$$

Then, because we have assumed the targets are independent, the total mutual information between all targets and all target states is simply the sum of its individual constituents, given as

$$\boldsymbol{I}(\boldsymbol{X}_{\mathrm{T}}; \boldsymbol{Y}) = \sum_{i=1}^{N_{\mathrm{T}}} \boldsymbol{I}^{(i)} \left(\boldsymbol{X}_{\mathrm{T}}^{(i)}; \boldsymbol{Y}^{(i)} \right), \tag{23}$$

where,

$$\boldsymbol{X}_{\mathrm{T}} = \left[\boldsymbol{X}_{\mathrm{T}}^{(1)}, \boldsymbol{X}_{\mathrm{T}}^{(2)}, \cdots, \boldsymbol{X}_{\mathrm{T}}^{(N_{\mathrm{T}})} \right], \tag{24}$$

$$\boldsymbol{Y} = \left[\boldsymbol{Y}^{(1)}, \boldsymbol{Y}^{(2)}, \cdots, \boldsymbol{Y}^{(N_{\mathrm{T}})} \right]. \tag{25}$$

For our application, the first form of the mutual information provided in Eq. 22 is preferable because, as described in Section III, we require repeated evaluations to determine its sensitivity with respect to the observer's position along the trajectory. This is only explicitly related through the measurement Jacobian matrices, which are solely contained to the block matrices $\tilde{S}^{(i)}$ and $\tilde{\Gamma}^{(i)}$. Therefore, the matrix inverse $\left(\tilde{P}^{(i)} \right)^{-1}$ needs only to be computed once. Furthermore, the matrix dimension in the numerator and denominator are significantly smaller than the other forms, so the determinant evaluation is more efficient and exhibits better numerical stability.

B. System Dynamics and Measurements

In this work, we use the CRTBP to model the natural motion of the targets and observer in the cislunar environment. The Earth and the moon are the primary bodies and revolve in circular arcs around the system barycenter. The CRTBP assumes that the effect of the third body (i.e., target or observer platform) is negligible on the first two bodies. Expressed in a synodic frame where the x-axis points from the system barycenter to the moon, the z-axis is oriented with the system's angular momentum vector, and the y-axis completes the right-hand-rule, the system is conservative and we can define a pseudo-potential function U as

$$U = \frac{1-\mu}{r_1} + \frac{\mu}{r_2} + \frac{1}{2}(x^2 + y^2). \tag{26}$$

In the above, $\mu = \frac{m_m}{m_m + m_E}$, where m_m is the mass of the moon and m_E is the mass of the Earth. r_1 is the distance of the third body from the Earth and r_2 is the distance of the third body to the moon, which are

$$r_1 = \sqrt{(x-\mu)^2 + y^2 + z^2}, \tag{27a}$$

$$r_2 = \sqrt{(x-\mu+1)^2 + y^2 + z^2}. \tag{27b}$$

5

The equations of motion for the third body can then be expressed as

$$\ddot{x} - \dot{y} - x = \frac{\partial U}{\partial x}, \tag{28a}$$

$$\ddot{y} + 2\dot{x} - y = \frac{\partial U}{\partial y}, \tag{28b}$$

$$\ddot{z} = \frac{\partial U}{\partial z}, \tag{28c}$$

and stated explicitly as vector of differential equations,

$$\boldsymbol{x}(t) = [x, y, z, \dot{x}, \dot{y}, \dot{z}]^\top, \tag{29a}$$

$$\boldsymbol{f}(\boldsymbol{x}, t) = [\dot{x}, \dot{y}, \dot{z}, \ddot{x}, \ddot{y}, \ddot{z}]^\top. \tag{29b}$$

The the continuous time dynamics Jacobian matrix is

$$A(t) = \begin{bmatrix} 0_{3\times3} & I_{3\times3} \\ H & 2J \end{bmatrix}, \tag{30}$$

where,

$$H = \begin{bmatrix} \frac{\partial^2 U}{\partial x^2} & \frac{\partial^2 U}{\partial x \partial y} & \frac{\partial^2 U}{\partial x \partial z} \\ \frac{\partial^2 U}{\partial y \partial x} & \frac{\partial^2 U}{\partial y^2} & \frac{\partial^2 U}{\partial y \partial z} \\ \frac{\partial^2 U}{\partial z \partial x} & \frac{\partial^2 U}{\partial z \partial y} & \frac{\partial^2 U}{\partial z^2} \end{bmatrix}, \quad J = \begin{bmatrix} 0 & 1 & 0 \\ -1 & 0 & 0 \\ 0 & 0 & 0 \end{bmatrix}. \tag{31}$$

It is sometimes convenient to formulate the distance and time scales for the CRTBP in normalized units and we interchange between normalized and SI units throughout the remainder of this paper. The distance between the two primary bodies (Earth and moon) is the distance unit (DU), and time unit (TU) is $\frac{T}{2\pi}$ where T is the period of the system around the barycenter.

Measurements from the optical sensor platform are modeled as angular longitude and latitude coordinates expressed in the synodic frame. These are given as

$$\boldsymbol{y} = \begin{bmatrix} \theta \\ \phi \end{bmatrix} = \begin{bmatrix} \tan^{-1}\left(\frac{\rho_y}{\rho_x}\right) \\ \sin^{-1}\left(\frac{\rho_z}{\|\boldsymbol{\rho}\|}\right) \end{bmatrix}, \tag{32}$$

where,

$$\boldsymbol{\rho} = \boldsymbol{r}_T - \boldsymbol{r}. \tag{33}$$

Here, $\boldsymbol{r}_T$ is the position of the target spacecraft and $\boldsymbol{r}$ is the position of the observer. The measurement Jacobian matrix in Eq. 16 is

$$H = \begin{bmatrix} -\frac{\rho_y}{\rho_{xy}^2} & \frac{\rho_x}{\rho_{xy}^2} & 0 & 0 & 0 & 0 \\ -\frac{\rho_x \rho_z}{\|\boldsymbol{\rho}\|^2 \rho_{xy}} & -\frac{\rho_y \rho_z}{\|\boldsymbol{\rho}\|^2 \rho_{xy}} & \frac{\rho_{xy}}{\|\boldsymbol{\rho}\|^2} & 0 & 0 & 0 \end{bmatrix}, \tag{34}$$

where,

$$\rho_{xy} = \sqrt{\rho_x^2 + \rho_y^2}. \tag{35}$$

III. Methodologies

A. Optimal Control Problem

In this section, we describe the form of the optimal control problem and the solution method used to solve it. For much of the discussion we adopt the notation used in [15] to describe our implementation of the SCvx algorithm; an SCP approach with global convergence and a superlinear convergence rate [14]. We find it a more natural progression to first introduce the problem in continuous time, and then illustrate how this continuous time optimal control problem is

transformed to discrete-time through direct collocation. At its core, this work solves a fixed-time, nonlinear, two-point boundary value problem:

$$\min_{\boldsymbol{u}(t)} J(\boldsymbol{x}(t), \boldsymbol{u}(t)) \tag{36a}$$

$$\text{s.t. } \dot{\boldsymbol{x}}(t) = \boldsymbol{f}(\boldsymbol{x}(t), \boldsymbol{u}(t), t), \tag{36b}$$

$$\boldsymbol{g}_{\text{ic}}(\boldsymbol{x}(0)) = \boldsymbol{0}, \tag{36c}$$

$$\boldsymbol{g}_{\text{tc}}(\boldsymbol{x}(t_f)) = \boldsymbol{0}, \tag{36d}$$

$$\|\boldsymbol{u}(t)\|_2 \leq a_{\max}. \tag{36e}$$

In the above, $\boldsymbol{x}(t)$ is the continous time representation of the state of the observer platform, $\boldsymbol{u}(t) = [u_x(t), u_y(t), u_z(t)]^\top$ is the continuous time control input vector, and $\boldsymbol{g}_{\text{ic}}(\cdot)$ and $\boldsymbol{g}_{\text{tc}}(\cdot)$ are the initial and terminal boundary conditions given as

$$\boldsymbol{g}_{\text{ic}}(\boldsymbol{x}(0)) = \boldsymbol{x}(0) - \boldsymbol{x}_{\text{ref}}(0), \tag{37a}$$

$$\boldsymbol{g}_{\text{tc}}(\boldsymbol{x}(t_f)) = \boldsymbol{x}(t_f) - \boldsymbol{x}_{\text{ref}}(t_f). \tag{37b}$$

$\boldsymbol{x}_{\text{ref}}$ is the reference trajectory for a passive (i.e., no thrust) observer, which, for this work, is selected as a periodic orbit in the CRTBP. The boundary conditions in Eq. 37 ensure the observer returns to the same periodic orbit after a fixed time interval, t_f. Eq. 36e sets an engineering constraint for the maximum thrust acceleration. We do not consider the effect of mass loss on the thrust acceleration during the planning window. However, the high specific impulse of low-thrust propulsion coupled with the relatively short (e.g., $1-3$ period) planning interval considered make this effect negligible in this study. The continuous time objective function used in this work is given as

$$J(\boldsymbol{x}(t), \boldsymbol{u}(t)) = (1 - \sigma_h) \int_0^{t_f} \|\boldsymbol{u}(t)\|_2 dt - \sigma_h \boldsymbol{I}(X_{\text{T}}; Y). \tag{38}$$

By varying the homotopy parameter, $\sigma_h \in [0, 1]$, we can control the relative weight placed between minimizing the control effort and maximizing the information gain of the observer. Note the negative sign distributed to the mutual information term in Eq. 38 which transforms its maximization into a minimization, consistent with Eq. 36a.

B. Dynamics Linearization and Discretization

We solve the nonlinear optimal control problem provided in Eq. 36 with a sequence of convex programs. For each iteration to be compatible with a convex solver, we must linearize the objective function and dynamics of the system around the previous iteration's solution. Let $\bar{\boldsymbol{x}}(t)$ and $\bar{\boldsymbol{u}}(t)$ denote a continuous time reference solution, then define a set of linearization variable as

$$A(t) := \frac{\partial \boldsymbol{f}(t, \bar{\boldsymbol{x}}(t), \bar{\boldsymbol{u}}(t))}{\partial \boldsymbol{x}(t)}, \tag{39a}$$

$$B(t) := \frac{\boldsymbol{f}(t, \bar{\boldsymbol{x}}(t), \bar{\boldsymbol{u}}(t))}{\partial \boldsymbol{u}(t)}, \tag{39b}$$

$$\boldsymbol{r}(t) := \boldsymbol{f}(t, \bar{\boldsymbol{x}}(t), \bar{\boldsymbol{u}}(t)) - A\bar{\boldsymbol{x}}(t) - B\bar{\boldsymbol{u}}(t). \tag{39c}$$

At each convex iteration, a local approximation of Eq. 36 is given as

$$\min_{\boldsymbol{u}} J(\boldsymbol{x}, \boldsymbol{u}) \tag{40a}$$

$$\text{s.t. } \dot{\boldsymbol{x}}(t) = A(t)\boldsymbol{x}(t) + B(t)\boldsymbol{u}(t) + \boldsymbol{r}(t), \tag{40b}$$

$$\boldsymbol{g}_{\text{ic}}(\boldsymbol{x}(0)) = \boldsymbol{0}, \tag{40c}$$

$$\boldsymbol{g}_{\text{tc}}(\boldsymbol{x}(t_f)) = \boldsymbol{0}, \tag{40d}$$

$$\|\boldsymbol{u}(t)\|_2 \leq a_{\max}, \tag{40e}$$

$$\|\delta\boldsymbol{x}(t)\|_2 + \|\delta\boldsymbol{u}(t)\|_2 \leq \eta. \tag{40f}$$

Linearization is only accurate in a local neighborhood of the reference solution, so Eq. 40f bounds each step where,

$$\delta\boldsymbol{x}(t) = \boldsymbol{x}(t) - \bar{\boldsymbol{x}}(t), \tag{41a}$$

$$\delta\boldsymbol{u}(t) = \boldsymbol{u}(t) - \bar{\boldsymbol{u}}(t). \tag{41b}$$

The bound η is iteratively adjusted at each iteration with a trust-region update discussed in Subsection III.D.

Using direct collocation involves transforming the corresponding infinite dimensional continuous-time optimal control problem into a finite dimensional static optimization. In this work, we a use first-order hold interpolation to discretize the problem at the time nodes $\{t_k\}_{k=1}^{N}$. The continuous time control input and linearized continuous time dynamics are then approximated between time nodes as

$$\boldsymbol{u}(t) = \frac{t_{k+1} - t}{t_{k+1} - t_k}\boldsymbol{u}_k + \frac{t - t_k}{t_{k+1} - t_k}\boldsymbol{u}_{k+1}$$

$$= \lambda_k^-(t)\boldsymbol{u}_k + \lambda_k^+(t)\boldsymbol{u}_{k+1}, \tag{42a}$$

$$\dot{\boldsymbol{x}}(t) = A(t)\boldsymbol{x}(t) + B(t)\lambda_k^-(t)\boldsymbol{u}_k + B(t)\lambda_k^+\boldsymbol{u}_{k+1} + \boldsymbol{r}(t), \tag{42b}$$

where $\boldsymbol{u}_k$ and $\boldsymbol{u}_{k+1}$ are control impulse vectors at times t_k and t_{k+1}, respectively. Following this, the corresponding discrete time state update is

$$\boldsymbol{x}_{k+1} = A_k\boldsymbol{x}_k + B_k^-\boldsymbol{u}_k + B_k^+\boldsymbol{u}_{k+1} + \boldsymbol{r}_k, \tag{43}$$

where,

$$A_k = \Phi(t_{k+1}, t_k), \tag{44a}$$

$$B_k^- = A_k \int_{t_k}^{t_{k+1}} \Phi(\tau, t_k)^{-1} B(\tau)\lambda_k^-(\tau)d\tau, \tag{44b}$$

$$B_k^+ = A_k \int_{t_k}^{t_{k+1}} \Phi(\tau, t_k)^{-1} B(\tau)\lambda_k^+(\tau)d\tau, \tag{44c}$$

$$\boldsymbol{r}_k = A_k \int_{t_k}^{t_{k+1}} \Phi(\tau, t_k)^{-1} \boldsymbol{r}(\tau)d\tau. \tag{44d}$$

In practice, we jointly compute the discrete-time variables in Eq. 44 by numerically integrating the following system of ordinary differential equations:

$$\boldsymbol{\Xi}(t) = \begin{bmatrix} \boldsymbol{x}(t) \\ \mathrm{flat}\big(\Phi(t, t_k)\big) \\ \mathrm{flat}\big(B_k^-(t)\big) \\ \mathrm{flat}\big(B_k^+(t)\big) \\ \boldsymbol{r}_k(t) \end{bmatrix}, \tag{45}$$

where,

$$\dot{\boldsymbol{\Xi}}(t) = \begin{bmatrix} \boldsymbol{f}(\boldsymbol{x}(t), \bar{\boldsymbol{u}}(t)) \\ \mathrm{flat}\big(A(t)\Phi(t, t_k)\big) \\ \mathrm{flat}\big(\Phi(t, t_k)^{-1}\lambda_k^-(t)B(t)\big) \\ \mathrm{flat}\big(\Phi(t, t_k)^{-1}\lambda_k^+(t)B(t)\big) \\ \Phi(t, t_k)^{-1}\boldsymbol{r}(t) \end{bmatrix}, \quad \boldsymbol{\Xi}(t_k) = \begin{bmatrix} \bar{\boldsymbol{x}}_k \\ \mathrm{flat}(I_{n_x \times n_x}) \\ 0_{n_x n_u \times 1} \\ 0_{n_x n_u \times 1} \\ 0_{n_x \times 1} \end{bmatrix}. \tag{46}$$

As discussed in [15], one feature of SCP algorithms is the phenomenon known as artificial infeasibility where the linearized path constraints do not admit a feasible solution, despite the original nonlinear problem being feasible. To handle this effect, SCvx makes the algorithmic choice to add a slack variable to each linearized constraint, which we denote ϵ_k. The slack variables are termed "virtual controls" and act to soften the constraint to allow dynamics feasibility until solution convergence. With this, the final form of the local convex optimization problem is

$$\min_{\boldsymbol{x}, \boldsymbol{u}, \boldsymbol{\epsilon}} \mathcal{L}(\boldsymbol{x}, \boldsymbol{u}, \boldsymbol{\epsilon}) \tag{47a}$$

$$\text{s.t. } \boldsymbol{x}_{k+1} = A_k\boldsymbol{x}_k + B_k^-\boldsymbol{u}_k + B_k^+\boldsymbol{u}_{k+1} + \boldsymbol{r}_k + E_k\boldsymbol{\epsilon}_k, \tag{47b}$$

$$\boldsymbol{g}_{\mathrm{ic}}(\boldsymbol{x}(0)) = \boldsymbol{0}, \tag{47c}$$

$$\boldsymbol{g}_{\mathrm{tc}}(\boldsymbol{x}(t_f)) = \boldsymbol{0}, \tag{47d}$$

$$\|\boldsymbol{u}_k\|_2 \le u_{max,k}, \tag{47e}$$

$$\|\delta\boldsymbol{x}_k\|_2 + \|\delta\boldsymbol{u}_k\|_2 \le \eta. \tag{47f}$$

Here, $\mathcal{L}(\cdot)$ is the linearized objective function which is further discussed in Subsection III.C. x, u, and ϵ denote the augmented discrete states, control inputs, and virtual controls along the trajectory arc, respectively. E_k is the discrete time virtual control gain matrix where its continuous time counterpart is $E(t) = I_{n_x \times n_x}$. E_k is computed by augmenting $\Xi(t)$ so that

$$\tilde{\Xi}(t) = \begin{bmatrix} \Xi(t) \\ \text{flat}(E_k(t)) \end{bmatrix}, \tag{48}$$

where,

$$\dot{\tilde{\Xi}}(t) = \begin{bmatrix} \dot{\Xi}(t) \\ \text{flat}(\Phi^{-1}(t, t_k) E(t)) \end{bmatrix}, \quad \tilde{\Xi}(t_k) = \begin{bmatrix} \Xi(t_k) \\ 0_{n_x n_x \times 1} \end{bmatrix}. \tag{49}$$

One of the primary computational bottlenecks in computing the terms in Eq. 49 is matrix inversion of the state transition matrix. As recognized in [16] this can be carried out efficiently with Gaussian elimination via LU decomposition, and we employ the same approach in this work.

C. Linearized Objective Function

For the final converged solution to be dynamically feasible, the virtual control variables, ϵ, must be driven to zero. To accomplish this, SCvx adds a penalty for the virtual control variables to the original objective. A trapezoid integration approximation jointly penalizes the control effort and virtual control variables which is given by

$$\mathcal{U}(u, \epsilon, \sigma_h) = \sum_{k=1}^{N-1} \frac{\Delta t_k}{2} \Big((1 - \sigma_h)(\|u_k\|_2 + \|u_{k+1}\|_2) + \gamma(\|E_k \epsilon_k\|_1 + \|E_{k+1} \epsilon_{k+1}\|_1) \Big). \tag{50}$$

In the above, $\Delta t_k = t_{k+1} - t_k$ and γ is a scalar chosen to be sufficiently large as to drive the virtual control variables to zero. Note that we only distribute the homotopy parameter, $1 - \sigma_h$, to the control effort term to ensure the virtual control penalty is not affected by this design choice.

It is necessary to linearize the problem's objective function so that each SCvx iteration is compatible with a convex program solver. To do this, the mutual information is approximated at each iteration step using a first-order Taylor series expansion around the reference solution:

$$\widehat{I}(X_\mathrm{T}; Y) = I(X_\mathrm{T}; \overline{Y}) + \frac{\partial I(X_\mathrm{T}; Y)}{\partial x} \delta x, \tag{51}$$

where $\overline{Y}$ are the measurements obtained from a sensing platform following the previous solution's trajectory, $\bar{x}$. The partial derivatives in Eq. 51 do not permit an analytic expression, but can be efficiently computed with automatic differentiation (AD). The choice of the AD approach can significantly affect the stability and computation time required in computing the gradient. Here, we use a reverse-mode AD algorithm implemented in the Zygote [21] package with Julia programming language. The final convex objective in Eq. 47 is then

$$\mathcal{L}(x, u, \epsilon) = \mathcal{U}(u, \epsilon, \sigma_h) + \sigma_h \widehat{I}(X; Y). \tag{52}$$

D. Trust Region Update

At each convex iteration, SCvx updates the trust region region radius, η, by comparing the linearized objective improvement in Eq. 52 with the true nonlinear objective improvement. To do this, a linearization defect vector is defined as

$$\delta_k = x_{k+1} - f_k(x_k, u_k, u_{k+1}), \tag{53}$$

where $f_k(\cdot)$ here is the true discrete time transitional dynamics between nodes k and $k+1$ with control input, and is found by numerically integrating Eq. 42b. A zero defect indicates that the converged solution is dynamically feasible. The true nonlinear cost is then

$$\mathcal{J}(x, u, \delta) = \mathcal{U}(u, \delta, \sigma_h) + \sigma_h I(X; Y), \tag{54}$$

and the expected improvement is compared with the actual improvement through a linearization accuracy metric defined as

$$\rho = \frac{\mathcal{J}(\bar{x}, \bar{u}, \bar{\delta}) - \mathcal{J}(x^*, u^*, \delta^*)}{\mathcal{J}(\bar{x}, \bar{u}, \bar{\delta}) - \mathcal{L}(x^*, u^*, \epsilon^*)}. \tag{55}$$

9

The variables with the superscript ($*$) denote those produced by each convex solver iteration. Depending on the accuracy metric, we update the reference states and trust region accordingly. These conditions are listed in Table 1 and correspond to those provided in [15]. The bounds ρ_0, ρ_1, and, ρ_2 are user defined variable in $[0, 1]$ and β_{sh}, β_{gr} are a trust region shrinkage and growth factors, respectively.

Table 1   Trust region update protocol

Case	Update Rule		
$\rho < \rho_0$	$\eta \rightarrow \eta/\beta_{\text{sh}}$	$\bar{x} \rightarrow \bar{x}$	$\bar{u} \rightarrow \bar{u}$
$\rho_0 \leq \rho < \rho_1$	$\eta \rightarrow \eta/\beta_{\text{sh}}$	$\bar{x} \rightarrow x^*$	$\bar{u} \rightarrow u^*$
$\rho_1 \leq \rho < \rho_2$	$\eta \rightarrow \eta$	$\bar{x} \rightarrow x^*$	$\bar{u} \rightarrow u^*$
$\rho_2 \leq \rho$	$\eta \rightarrow \beta_{\text{gr}}\eta$	$\bar{x} \rightarrow x^*$	$\bar{u} \rightarrow u^*$

E. Selection of Discrete Nodes

An important component relating to the reliability of SCvx for our problem is the effective spacing of collocation nodes. A simple but naive approach is to place nodes equally in time, however, in highly nonlinear intervals of the reference trajectory, the linear approximations used by SCvx begin to break down. There are several more informative options. In [19] the authors choose an adaptive discretization using a variable step numerical integrator. In this work, we follow the procedure used in [22], employing the generalized Sundman transformation [23]. This acts as a physically informed step-size regulator by transforming the time variable to a new variable, τ, defined here as

$$dt = r_m^\alpha d\tau. \tag{56}$$

In the above, r_m is the distance of the observer from the moon, and α is a user-defined parameter. When $\alpha = 0$ we see that the time variable is indeed equivalent to τ, but increasing α effectively dilates time in regions closer to perilune, as shown in Fig. 2a.

In implementation, we determine the time node spacing by numerically integrating

$$\frac{dz}{d\tau} = r_m^\alpha \begin{bmatrix} f(x, \tau) \\ 1 \end{bmatrix}, \tag{57}$$

where,

$$z(\tau) = [x^\top(\tau), t]^\top, \tag{58}$$

and output the time variable at equally spaced $\{\tau_k\}_{k=1}^N$. In Fig. 1 we show the effect of the Sundman transformation in spacing the collocation nodes for an NRHO reference orbit with initial conditions defined in Table 5. The top panels show the projected orbit when nodes are spaced equally in time, $\alpha = 0.0$, and the bottom show the orbit with a regularization parameter where $\alpha = 1.1$. In regions closer perilune, regularization ensures that nodes are spaced more uniformly to capture the true motion of the observer. Because the time is not equivalent between nodes, to correctly model the thrust constraint in Eq. 47e we must find $u_{\text{max},k}$ consistent with the obtainable impulse between collocation points. For each point, this can be written as

$$\frac{u_{\text{max},k} + u_{\text{max},k+1}}{2\Delta t_k} = a_{\text{max}}, \tag{59}$$

and can be solved at all nodes with,

$$\begin{bmatrix} 1/\Delta t_1 & 1/\Delta t_1 & 0 & \cdots & 0 & 0 \\ 0 & 1/\Delta t_2 & 1/\Delta t_2 & \cdots & 0 & 0 \\ \vdots & \vdots & \ddots & \ddots & \vdots & \vdots \\ 0 & 0 & \cdots & 0 & 1/\Delta t_{N-1} & 1/\Delta t_{N-1} \end{bmatrix} \begin{bmatrix} u_{\text{max},1} \\ u_{\text{max},2} \\ \vdots \\ u_{\text{max},N} \end{bmatrix} = 2a_{\text{max}} \begin{bmatrix} 1 \\ 1 \\ \vdots \\ 1 \end{bmatrix}. \tag{60}$$

Eq. 60 is an underdetermined linear system of equations and its minimum norm solution can be found efficiently with a QR factorization.
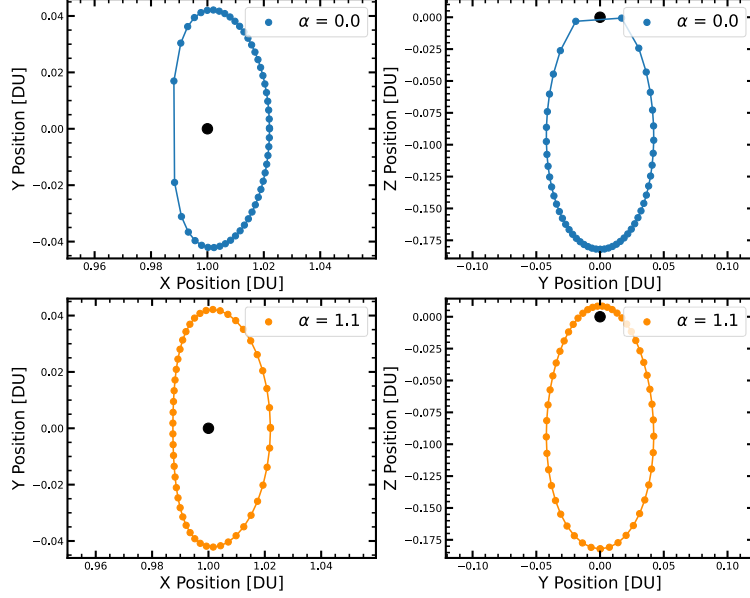
10

Fig. 1   Effect of the variable transformation on position node spacing for a reference NRHO.
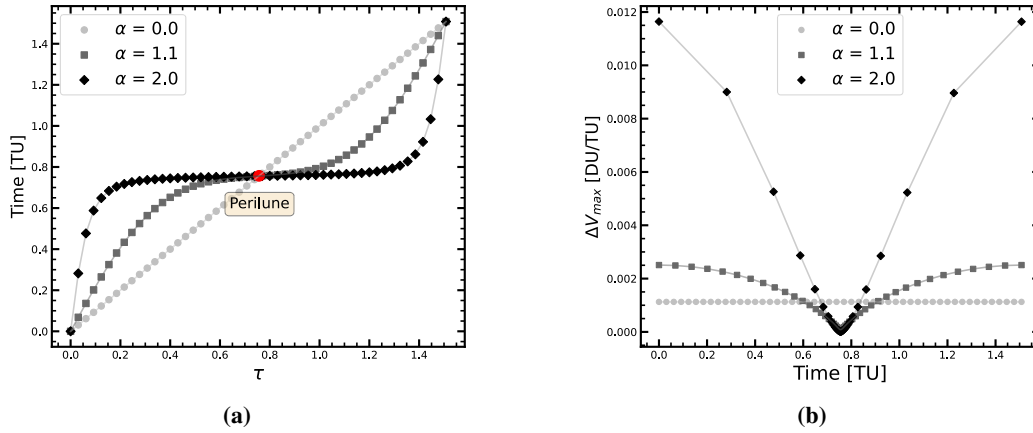

| (a) | (b) |

Fig. 2   Effect of the variable transformation on time spacing and $u_{\mathbf{max},k}$ for a reference NRHO.

F. Selection of Measurement Nodes

As noted previously, the measurement times for the observer do not directly correspond to all discrete time nodes. Ideally, we would like to model the measurements evenly in time. If the discretization is sufficiently dense, then a nearest neighbors approximation is adequate for finding the measurement times as a subset of all discrete time nodes. We employ this approach in this study. Let f_{meas} correspond to the measurement cadence frequency of the observer. Then, a uniform grid spacing of measurements is

$$\{t_\ell\}_{\ell=1}^{N_{\text{meas}}} = [0, 1/f_{\text{meas}}, 2/f_{\text{meas}}, \cdots, N_{\text{meas}}/f_{\text{meas}}], \tag{61}$$

where,

$$N_{\text{meas}} = \text{floor}\left(\frac{t_f}{f_{\text{meas}}}\right), \tag{62}$$

and the floor($\cdot$) operator returns the greatest integer less than the argument. The measurement time selected for each grid point index, l, is then given as

$$t_{k'} = \arg\min_{t_k} |t_\ell - t_k|, \text{ for } t_k \in \{t_k\}_{k=1}^N, \tag{63}$$

11

so that the full set of measurement times as a subset of the discretization nodes are

$$\{t_{k'}\}_{k'=1}^{N_{\text{meas}}}. \tag{64}$$

IV. Numerical Simulations

In this section, we demonstrate several numerical simulations to evaluate our approach. The software in written in the Julia programming language. For each SCvx iteration, we use the embedded conic solver (ECOS) [24] which is an interior-point solver for second-order conic programming. To interface with the solver we use `Convex` [25], which is a Julia package for Disciplined Convex Programming (DCP). For each test case, one or two targets are initially placed in close proximity to the reference orbit of the observer. For all of the test cases, we use the hyperparameters listed in Table 2 including those informed by the scenario (i.e., thrust constraint, measurement cadence, etc.) and those relating our SCvx implementation. The initialization of decision variables for all test cases is taken to be a purely passive observer along the reference trajectory.

Table 2   Algorithm parameters used for all simulations

Parameter	Symbol	Value
Discrete nodes	N	300
Sundman Regularization	α	1.1
Distance Unit	DU [km]	384400.0
Time Unit	TU [days]	4.34
Maximum Thrust	a_{max} [km/s^2]	1×10^{-7}
Measurement Cadence	f_{meas} [1/day]	1.0
Process Noise PSD	Q [km/s^3]	$1 \times 10^{-10} I_{3 \times 3}$
Measurement Noise Covariance	R [rad^2]	$1 \times 10^{-10} I_{2 \times 2}$
Virtual Control Penalty	γ	1×10^6
Convexification Accuracy	ρ_0	0.0
	ρ_1	0.1
	ρ_2	0.7
Initial Trust Region	η_0	0.1
Trust Region Shrinkage	β_{sh}	1.5
Trust Region Growth	β_{gr}	1.5

Our first test case considers a single-target tracking problem in which an observer is placed on a DRO. The test case properties are listed in Table 3. In the CRTBP, a DRO is a planar orbit with little nonlinearity when compared to other periodic orbits. Its stability and geometric properties make it ideal for a variety of cislunar mission architectures. The observer is placed at the conditions corresponding to the reference DRO and must return to those after two orbit periods. The target has a small in-plane and out-of-plane deviation with respect to the reference orbit in position and no deviation in velocity. We assume that the observer collects one angular bearing measurement per day. The target has an initial uncertainty of 100.0 km standard deviation in each position coordinate and 0.001 km/s in velocity.

In Fig. 3a we show the flight path of an optimized observer. Here, and in all following figures, we are plotting in a frame centered at the target with coordinates in the same basis as the synodic frame. Additionally, the green and red markers correspond to the initial and terminal positions of the observer, respectively. The blue quivers indicate the thrust magnitude and direction. The flight path is also projected onto each plane of the reference frames, indicated by the gray curves.

In Fig. 3b we plot individually the projection of the observer's flight path for a spectrum of convex objective functions, where a purely passive observer corresponds to $\sigma_h = 0.0$. These figures elucidate the effect of the mutual information objective on the observer spacecraft. Intuitively, when $\sigma_h = 0.0$, the optimal solution is to perform no maneuvering, as this corresponds to the minimum control effort solution. Increasing the homotopy parameter directs the observer spacecraft to "loiter" around the target. This also has an intuitive interpretation because, in this case, the

Table 3   Parameters for the first DRO test case

Parameter	Symbol	Value
Observer Initial Conditions	$[x, y, z]^\top$ [DU]	$[0.80566, 0.0, 0.0]^\top$
	$[v_x, v_y, v_z]^\top$ [DU/TU]	$[0.0, 0.51947, 0.0]^\top$
Reference Period	T [TU]	3.20642
Time Interval	t_f [TU]	6.41284
Number of Targets	N_T	1
Target Initial Deviation	$[\Delta x, \Delta y, \Delta z]^\top$ [km]	$[200.0, 200.0, 100.0]^\top$
	$[\Delta v_x, \Delta v_y, \Delta v_z]^\top$ [km/s]	$[0.0, 0.0, 0.0]^\top$
Target Initial Uncertainty	$[\sigma_x, \sigma_y, \sigma_z]^\top$ [km]	$[100.0, 100.0, 100.0]^\top$
	$[\sigma_{v_x}, \sigma_{v_y}, \sigma_{v_z}]^\top$ [km/s]	$[0.001, 0.001, 0.001]^\top$

(a)   (b)

Fig. 3   Flight path of the optimized and passive observers for the DRO test case described in Table 3.

same change in the relative position between target and observer results in a larger amplification of geometric diversity in angular bearing measurements, increasing the system's observability.

Fig. 4 shows the thrust acceleration profile of the observer spacecraft in each direction and magnitude of the thrust acceleration over the observation window. The left-hand side shows the profile for $\sigma_h = 0.14$ and the right for the case where $\sigma_h = 0.17$. The profile closely resemble that from a minimum thrust targeting problem, excluding the portion between 12 and 15 days for $\sigma_h = 0.14$ case. The resemblance can be attributed to the inclusion of the thrust acceleration magnitude in our objective function which incentivizes this type of solution. Increasing the σ_h from 0.14 to 0.17 places more emphasis towards the information gain, and as a result, increases the cumulative control effort of the observer over the flight duration, 0.112 km/s versus 0.189 km/s.

While the mutual information provides a mechanism in formulating an objective function based on the performance of a sequential filter, it is valuable to evaluate the performance of the optimized observer over the course of the entire planning window. The Cramer-Rao lower bound (CRLB) provides a sequential estimators theoretical optimal performance along the entire trajectory, and we use it in this section to evaluate the efficacy of the mutual information as objective function for our information collection problem. For a nonlinear system where both the process noise and measurement noise are Gaussian, the extended Kalman filter covariance propagation and update equations, when linearized around the true state of the target, provide the CRLB [26]. In Fig. 5 we show the CRLB of the optimized
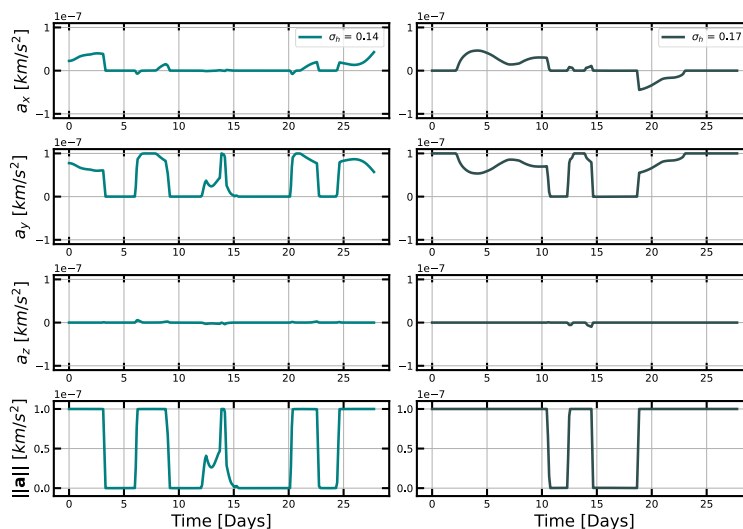
13

Fig. 4 Thrust acceleration profile for the DRO test case described in Table 3. The left- and right-hand sides correspond to a $\sigma_h = 0.14$ and $\sigma_h = 0.17$, respectively.

observer with increasing σ_h for each of the position coordinates. By increasing the relative weight of the mutual information in our objective, on average, we see a smaller theoretical lower bound for the RMS error of a sequential estimator. For this test case, in particular portions of the trajectory, the CRLB is reduced up to two orders of magnitude. One can note the similarities in the CRLB between all observers during the start and terminal sections of the trajectory. As stated, for our problem formulation, the boundary conditions enforce the observer to begin and terminate along the passive reference trajectory and so the geometry of the observer with respect to the targets is quite similar between all values of σ_h for these portions.
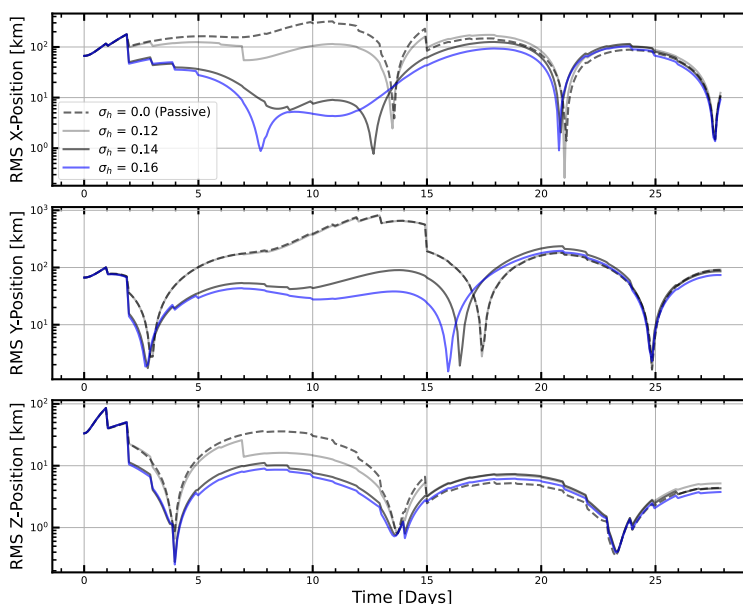
Fig. 5 CRLB analysis over a variety of homotopy parameters for the DRO test case in Table 3.

The second test case that we demonstrate, the observer is again placed on the DRO described in Tab. 3, but we consider the problem of simultaneously tracking two targets. The conditions for this case are listed in Table 4. Like the first test case, in Fig. 6 we show the flight path of the observer, but with the left- and right-hand sides shown centered around the flight path of the first and second target, respectively. Similarly, Fig. 7 shows the projected flight path

14

Table 4   Parameters for the second DRO test case

Parameter	Symbol	Value
Observer Initial Conditions	$[x, y, z]^\top$ [DU]	$[0.80566, 0.0, 0.0]^\top$
	$[v_x, v_y, v_z]^\top$ [DU/TU]	$[0.0, 0.51947, 0.0]^\top$
Reference Period	T [TU]	3.20642
Time Interval	t_f [TU]	6.41284
Number of Targets	N_T	2
Target #1 Initial Deviations	$[\Delta x, \Delta y, \Delta z]^\top$ [km]	$[175.0, 10.0, -30.0]^\top$
	$[\Delta v_x, \Delta v_y, \Delta v_z]^\top$ [km/s]	$[0.0, 0.0, 0.0]^\top$
Target #2 Initial Deviations	$--$	$[25.0, 400.0, 30.0]^\top$
	$--$	$[0.0, 0.0, 0.0]^\top$
Target #1 Initial Uncertainties	$[\sigma_x, \sigma_y, \sigma_z]^\top$ [km]	$[100.0, 100.0, 100.0]^\top$
	$[\sigma_{v_x}, \sigma_{v_y}, \sigma_{v_z}]^\top$ [km/s]	$[0.001, 0.001, 0.001]^\top$
Target #2 Initial Uncertainties	$--$	$[100.0, 100.0, 100.0]^\top$
	$--$	$[0.001, 0.001, 0.001]^\top$

(a)

(b)
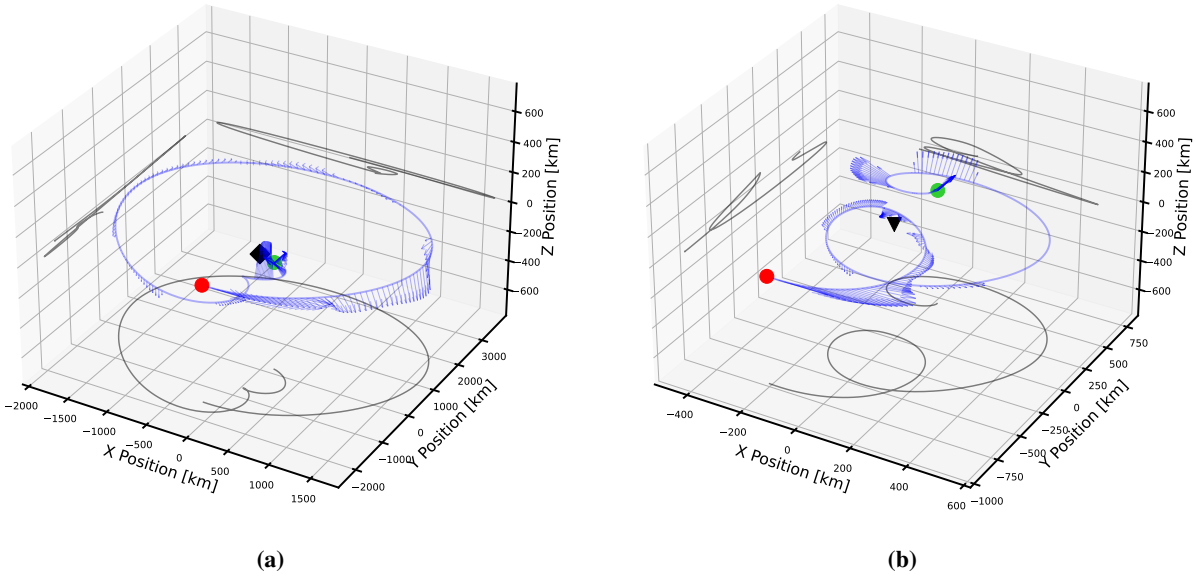
Fig. 6   Flight path of the optimized and passive observers for the DRO test case described in Table 4. The left- and right-hand sides correspond to the first and second target, respectively.

solution in each of the principal coordinate planes. Like the first test case, in the $x - y$ plane, it is apparent that the observer tends to linger around each of the targets. However, the out-of-plane motion exhibits an interesting behavior. Unlike the solutions shown in the first test case, increasing the homotopy parameter does not transition towards closer inspection of either target. We postulate that the inclusion of multiple targets into the tracking problem is well balanced by the mutual information objective which prefers a less optimal solution for either target in order to maximize the mutual information of the entire system. In Fig. 8 we show the thrust acceleration profile of two solutions, $\sigma_h = 0.18$ and $\sigma_h = 0.28$. Like before, during much of the flight path, the profile mimics that of a minimum thrust targeting problem. Increasing the homotopy parameter commensurately increases the cumulative control effort over the entire trajectory. The cumulative impulse for $\sigma_h = 0.18$ and $\sigma_h = 0.28$ cases is 0.066 km/s and 0.111 km/s, respectively. Fig. 9 shows a CRLB analysis for the first (left) and second (right) with increasing σ_h. As before, improved performance is
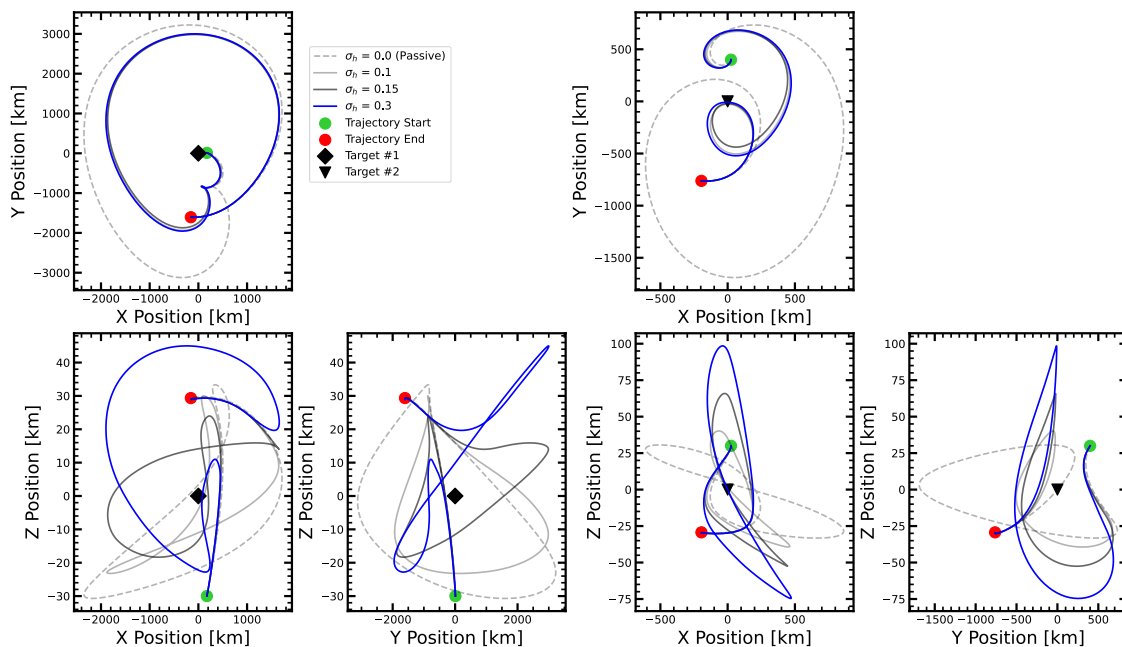
15

Fig. 7   Projected flight path of the optimized and passive observers for the DRO test case described in Table 4. The left- and right-hand sides correspond to the the first and second target, respectively.
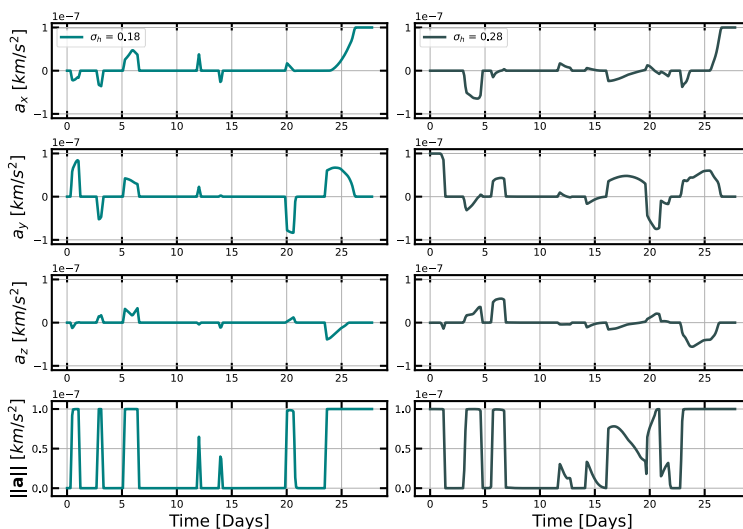

Fig. 8   Thrust acceleration profile for the DRO test case described in Table 4. The left- and right-hand sides correspond to a $\sigma_h = 0.18$ and $\sigma_h = 0.28$, respectively.

achieved by increasing the relative weight placed on maximizing the mutual information.

The third test case that we consider is a single target tracking scenario where the observer is situated on a NRHO reference trajectory with the scenario conditions listed in Table 5. Here, the observer is tasked with planning over a three period window. Like DROs, NRHOs exhibit favorable stability conditions and are well suited for future cislunar missions. However, unlike the previous DRO test cases, here the test case contains a close perilune passage. In this region, the reference trajectory exhibits stronger nonlinearities so it constitutes a more challenging test case for the SCvx algorithm. Fig. 10 again shows the flight paths for the passive and optimized observers. Unlike previously, the relative motion exhibits a large out-of-plane components, however, the overall behavior of the observer is similar; by increasing the importance of mutual information, the observer tends to linger closer to the target. Fig. 11 shows the
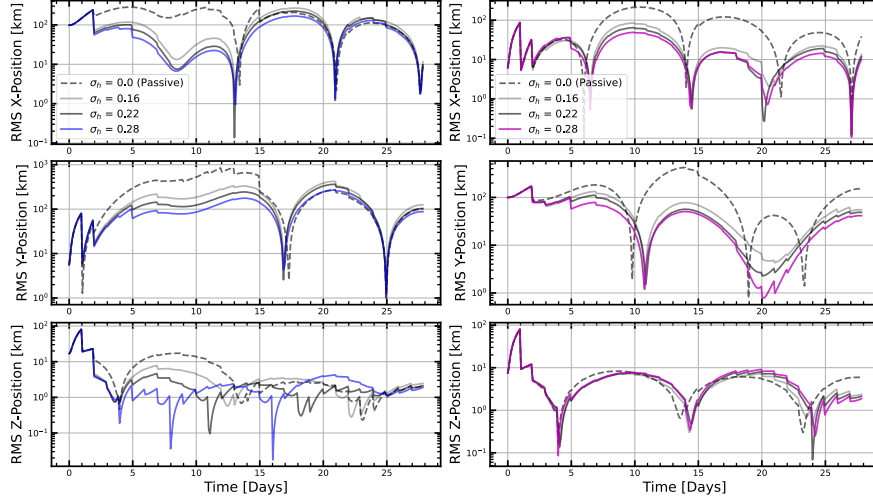
Fig. 9   CRLB analysis over a variety of homotopy parameters for the two-target DRO test case in Table 4. The left- and right-hand sides correspond to the estimation performance for the first and second target, respectively.

Table 5   Parameters for the NRHO test case

Parameter	Symbol	Value
Observer Initial Conditions	$[x, y, z]^\top$ [DU]	$[1.02202, 0.0, -0.18210]^\top$
	$[v_x, v_y, v_z]^\top$ [DU/TU]	$[0.0, -0.10326, 0.0]^\top$
Reference Period	T [TU]	3.20642
Time Interval	t_f [TU]	6.41284
Number of Targets	N_T	1
Target Initial Deviation	$[\Delta x, \Delta y, \Delta z]^\top$ [km]	$[200.0, 100.0, 0.0]^\top$
	$[\Delta v_x, \Delta v_y, \Delta v_z]^\top$ [km/s]	$[0.0, 0.0, 0.0]^\top$
Target Initial Uncertainty	$[\sigma_x, \sigma_y, \sigma_z]^\top$ [km]	$[100.0, 100.0, 100.0]^\top$
	$[\sigma_{v_x}, \sigma_{v_y}, \sigma_{v_z}]^\top$ [km/s]	$[0.001, 0.001, 0.001]^\top$

thrust acceleration profile for two cases where $\sigma_h = 0.15$ and $\sigma_h = 0.3$, corresponding to a cummulative impulse of 0.145 km/s and 0.215 km/s, respectively. Unlike the previous test case, there is a strong out-of-plane acceleration commanded throughout the duration of the planning window. In Fig. 12 we show the CRLB analysis for this case.

V. Conclusions

In this work, we introduce a trajectory planning tool for optimal relative orbit determination in the cislunar environment compatible with a low-thrust optical observer platform. Our approach uses a mutual information-based objective to optimally plan a trajectory that maximizes the targets' information gain conditioned on angular bearing measurements. We first derived a form of the mutual information using linearized/Gaussian assumptions. We also summarize the equations of motion and the measurement model for an optical observer operating in cislunar space. Following this, we described our implementation of the SCvx algorithm: a direct collocation method for solving our optimal control problem. We formulate the scenario as a fixed-time two point boundary value problem, where the objective of an observer spacecraft is to optimize a convex combination of the control effort and the mutual information. The necessary steps for implementation are provided. A physically-informed method for spacing collocation nodes based on the generalized Sundman transformation is also included in this discussion. This discretization scheme better facilitates convergence of our SCvx approach. Finally, we demonstrate the performance of our algorithm for several synthetic numerical case studies. These include single- and two-object tracking scenarios situated around DRO and NRHO period orbits. We point out salient features in the behavior of the observer spacecraft and demonstrate that the
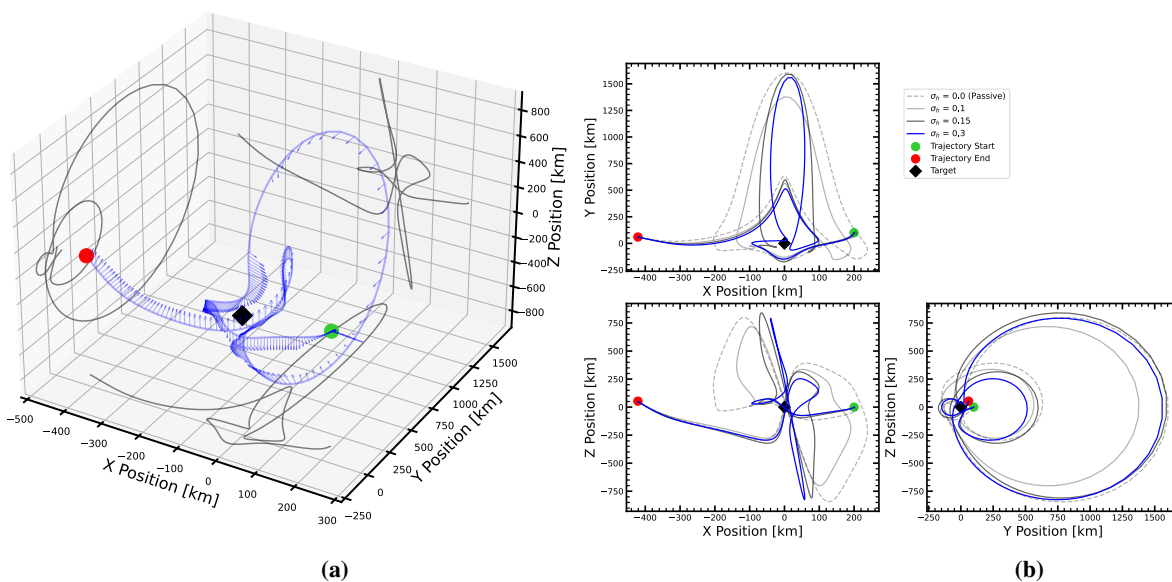
Fig. 10   Flight path of the optimized and passive observers for the NRHO test case described in Table 5.
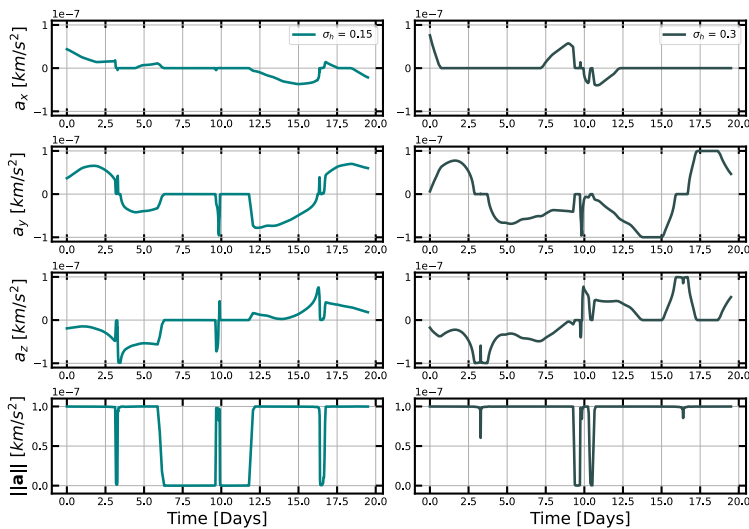

Fig. 11   Thrust acceleration profile for the NRHO test case described in Table 5. The left- and right-hand sides correspond to a $\sigma_h = 0.15$ and $\sigma_h = 0.3$, respectively.

theoretical estimation performance can be improved by several orders of magnitude in particular regions of a trajectory arc with respect to a purely passive observer.

There are several potential avenues for follow-up work. For simplicity, in this study we assumed that measurements are collected synchronously for all targets, however this assumption is only an approximation of the true information collection problem. Future work should address methods for jointly scheduling measurements while maneuvering. Furthermore, while we propose that our approach may be applicable to on-board planning operations, this study does not sufficiently address its feasibility. The compatibility of this approach with the computational resources of real flight hardware should be investigated. The CRTBP provides a convenient test-bed that captures the dominate dynamical modes in the cislunar environment, however our approach should be transitioned to a full ephemeris model as well. Finally, while we only consider the single-agent optimization problem, it would be useful to adapt our methods to multiple sensing agents through the lens of a cooperative game theoretic approach.
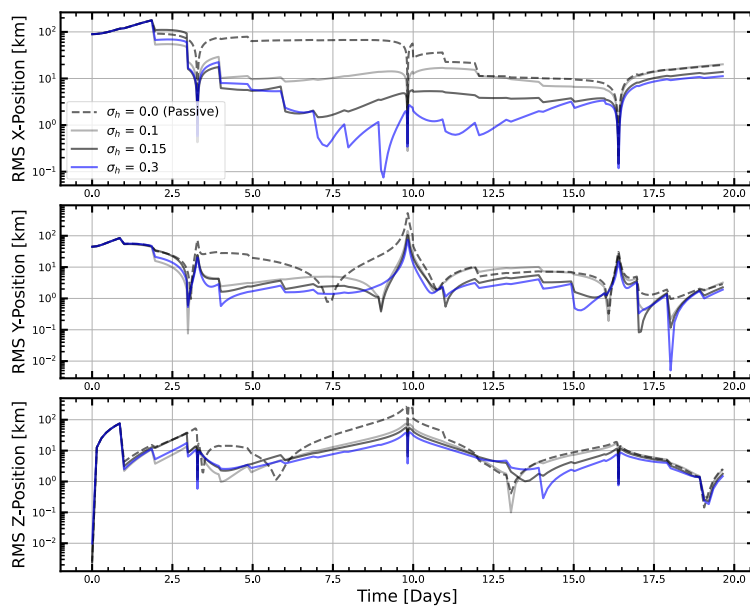
Fig. 12   CRLB analysis over a variety of homotopy parameters for the single target NRHO test case in Table 5.

Acknowledgements

References

[1] Parr, S., Wirwille, S., MacDonald, B., and Fowler, E., "Cislunar Security National Technical Vision," , Nov. 2019.

[2] Psiaki, M. L., "Gaussian-mixture Kalman filter for orbit determination using angles-only data," *Journal of Guidance, Control, and Dynamics*, Vol. 40, No. 9, 2017, pp. 2341–2347.

[3] Sullivan, J., and D'Amico, S., "Nonlinear Kalman filtering for improved angles-only navigation using relative orbital elements," *Journal of Guidance, Control, and Dynamics*, Vol. 40, No. 9, 2017, pp. 2183–2200.

[4] Bradley, N., Olikara, Z., Bhaskaran, S., and Young, B., "Cislunar Navigation Accuracy Using Optical Observations of Natural and Artificial Targets," *Journal of Spacecraft and Rockets*, Vol. 57, No. 4, 2020, pp. 777–792. https://doi.org/10.2514/1.A34694, URL https://doi.org/10.2514/1.A34694.

[5] Yun, S., Tuggle, K., Zanetti, R., and D'Souza, C., "Sensor Configuration Trade Study for Navigation in Near Rectilinear Halo Orbits," *Journal of the Astronautical Sciences*, Vol. 67, No. 4, 2020, pp. 1755–1774. https://doi.org/10.1007/s40295-020-00224-1.

[6] Vendl, J. K., and Holzinger, M. J., "Cislunar Periodic Orbit Analysis for Persistent Space Object Detection Capability," *Journal of Spacecraft and Rockets*, Vol. 58, No. 4, 2021, pp. 1174–1185. https://doi.org/10.2514/1.A34909, URL https://doi.org/10.2514/1.A34909.

[7] Fawcett, J., "Effect of course maneuvers on bearings-only range estimation," *IEEE Transactions on Acoustics, Speech, and Signal Processing*, Vol. 36, No. 8, 1988, pp. 1193–1199. https://doi.org/10.1109/29.1648.

[8] Woffinden, D. C., and Geller, D. K., "Optimal Orbital Rendezvous Maneuvering for Angles-Only Navigation," *Journal of Guidance, Control, and Dynamics*, Vol. 32, No. 4, 2009, pp. 1382–1387. https://doi.org/10.2514/1.45006, URL https://doi.org/10.2514/1.45006.

[9] Grzymisch, J., and Fichter, W., "Analytic Optimal Observability Maneuvers for In-Orbit Bearings-Only Rendezvous," *Journal of Guidance, Control, and Dynamics*, Vol. 37, No. 5, 2014, pp. 1658–1664. https://doi.org/10.2514/1.G000612, URL https://doi.org/10.2514/1.G000612.

[10] Hammel, S., Liu, P., Hilliard, E., and Gong, K., "Optimal observer motion for localization with bearing measurements," *Computers Mathematics with Applications*, Vol. 18, No. 1, 1989, pp. 171–180. https://doi.org/https://doi.org/10.1016/0898-1221(89)90134-X, URL https://www.sciencedirect.com/science/article/pii/089812218990134X.

[11] Oshman, Y., and Davidson, P., "Optimization of observer trajectories for bearings-only target localization," *IEEE Transactions on Aerospace and Electronic Systems*, Vol. 35, No. 3, 1999, pp. 892–902. https://doi.org/10.1109/7.784059.

[12] Hou, B., Wang, D., Wang, J., Ge, D., Zhou, H., and Zhou, X., "Optimal Maneuvering for Autonomous Relative Navigation Using Monocular Camera Sequential Images," *Journal of Guidance, Control, and Dynamics*, Vol. 44, No. 11, 2021, pp. 1947–1960. https://doi.org/10.2514/1.G005706, URL https://doi.org/10.2514/1.G005706.

[13] Adurthi, N., Singla, P., and Majji, M., "Mutual Information Based Sensor Tasking with Applications to Space Situational Awareness," *Journal of Guidance, Control, and Dynamics*, Vol. 43, No. 4, 2020, pp. 767–789. https://doi.org/10.2514/1.G004399, URL https://doi.org/10.2514/1.G004399.

[14] Mao, Y., Szmuk, M., Xu, X., and Acikmese, B., "Successive Convexification: A Superlinearly Convergent Algorithm for Non-convex Optimal Control Problems," *arXiv e-prints*, 2018, arXiv:1804.06539. https://doi.org/10.48550/arXiv.1804.06539.

[15] Malyuta, D., Reynolds, T. P., Szmuk, M., Lew, T., Bonalli, R., Pavone, M., and Açıkmeşe, B., "Convex Optimization for Trajectory Generation: A Tutorial on Generating Dynamically Feasible Trajectories Reliably and Efficiently," *IEEE Control Systems Magazine*, Vol. 42, No. 5, 2022, pp. 40–113. https://doi.org/10.1109/MCS.2022.3187542.

[16] Reynolds, T., Malyuta, D., Mesbahi, M., Acikmese, B., and Carson, J. M., "A real-time algorithm for non-convex powered descent guidance," *AIAA Scitech 2020 Forum*, 2020, p. 0844.

[17] Blackmore, L., Açıkmeşe, B., and Scharf, D. P., "Minimum-Landing-Error Powered-Descent Guidance for Mars Landing Using Convex Optimization," *Journal of Guidance, Control, and Dynamics*, Vol. 33, No. 4, 2010, pp. 1161–1171. https://doi.org/10.2514/1.47202, URL https://doi.org/10.2514/1.47202.

[18] Morgan, D., Chung, S.-J., and Hadaegh, F. Y., "Model Predictive Control of Swarms of Spacecraft Using Sequential Convex Programming," *Journal of Guidance, Control, and Dynamics*, Vol. 37, No. 6, 2014, pp. 1725–1740. https://doi.org/10.2514/1.G000218, URL https://doi.org/10.2514/1.G000218.

[19] Kayama, Y., Howell, K. C., Bando, M., and Hokamoto, S., "Low-Thrust Trajectory Design with Successive Convex Optimization for Libration Point Orbits," *Journal of Guidance, Control, and Dynamics*, Vol. 45, No. 4, 2022, pp. 623–637. https://doi.org/10.2514/1.G005916, URL https://doi.org/10.2514/1.G005916.

[20] Manning, C. D., *An introduction to information retrieval*, Cambridge university press, 2009.

[21] Innes, M., Edelman, A., Fischer, K., Rackauckas, C., Saba, E., Shah, V. B., and Tebbutt, W., "A Differentiable Programming System to Bridge Machine Learning and Scientific Computing," *arXiv e-prints*, 2019, arXiv:1907.07587. https://doi.org/10.48550/arXiv.1907.07587.

[22] Cunningham, D., and Russell, R., "An Interpolated Second-Order Relative Motion Model for Gateway," *Journal of the Astronautical Sciences*, Vol. 70, No. 4, 2023, 26. https://doi.org/10.1007/s40295-023-00393-9.

[23] Szebehely, V., and Grebenikov, E., "Theory of Orbits-The Restricted Problem of Three Bodies." *Soviet Astronomy, Vol. 13, p. 364*, Vol. 13, 1969, p. 364.

[24] Domahidi, A., Chu, E., and Boyd, S., "ECOS: An SOCP solver for embedded systems," *2013 European control conference (ECC)*, IEEE, 2013, pp. 3071–3076.

[25] Udell, M., Mohan, K., Zeng, D., Hong, J., Diamond, S., and Boyd, S., "Convex Optimization in Julia," *SC14 Workshop on High Performance Technical Computing in Dynamic Languages*, 2014.

[26] Taylor, J. H., "The Cramer-Rao estimation error lower bound computation for deterministic nonlinear systems," *1978 IEEE Conference on Decision and Control including the 17th Symposium on Adaptive Processes*, 1978, pp. 1178–1181. https://doi.org/10.1109/CDC.1978.268121.